Contents lists available at ScienceDirect

Ceramics International

journal homepage: www.elsevier.com/locate/ceramint

Electrical and electrochemical studies of nanocrystalline mesoporous MgFe$_2$O$_4$ as anode material for lithium battery applications

D. Narsimulu [a], B. Nageswara Rao [b], M. Venkateswarlu [c], E.S. Srinadhu [d], N. Satyanarayana [a,*]

[a] Department of Physics, Pondicherry University, Puducherry, 605014 India
[b] Department of Sciences & Humanities, Vignan's University, Vadlamudi, A.P., 522213 India
[c] R&D, Amara Raja Batteries Ltd, Karakambadi, A.P., 517520 India
[d] Department of Physics & Astronomy, Clemson University, Clemson, SC, 29634 USA

ARTICLE INFO

ABSTRACT

Nanocrystalline mesoporous spinel magnesium ferrite (MgFe$_2$O$_4$) particles with high surface area were prepared by urea assisted modified citrate combustion process. The prepared sample was characterized by X-ray diffraction (XRD), Fourier transform infrared (FTIR) spectroscopy, Raman spectroscopy, field-emission scanning electron microscope (FE-SEM), BET surface area analyzer and impedance spectroscopy techniques. XRD results confirmed the formation of a single phase of nanocrystalline spinel magnesium ferrite sample. FTIR and Raman spectroscopy (FTIR) results confirmed the structural co-ordination of the magnesium ferrite sample. The spherical shape morphology of the prepared magnesium ferrite particles was confirmed from the FE-SEM images. Specific surface area and porosity of the MgFe$_2$O$_4$ sample were obtained from N$_2$ adsorption–desorption isotherms results. The D.C. and A.C. electrical conductivities of the MgFe$_2$O$_4$ sample as a function of temperature and frequency were investigated by analyzing the measured impedance data. The activation energy for the migration of the carriers in the MgFe$_2$O$_4$ sample was found to be 0.607 eV. The dielectric studies revealed that the dielectric constant of the mesoporous MgFe$_2$O$_4$ sample increases with increase in temperature. Further, lithium battery was fabricated using the developed nanocrystalline mesoporous spinel MgFe$_2$O$_4$ as anode material and investigated its electrochemical performance. The charge-discharge studies revealed that the fabricated lithium battery using the developed nanocrystalline mesoporous MgFe$_2$O$_4$ as anode exhibited high capacity and good cycleability in the voltage range 0.005–3 V. The results show that the developed nanocrystalline mesoporous spinel magnesium ferrite could be a better anode material for lithium battery applications.

© 2016 Published by Elsevier Ltd and Techna Group S.r.l.

1. Introduction

Spinel ferrites with general formula MFe$_2$O$_4$ (M=Co^{+2}, Mg^{+2}, Cu^{+2}, etc.) are in great interest owing to their wide range of applications, such as electric, magnetic, adsorption, sensors, bio sensors, energy storage devices, magnetic storage devices, optics, drug delivery, etc. [1–8]. Among them, magnesium ferrite (MgFe$_2$O$_4$) has cubic spinel structure along with partially inverse spinel structure, which is due to the occupation of the fraction of Fe^{+3} ions in the octahedral sites [9]. Also, MgFe$_2$O$_4$ is a soft magnet having n-type semiconducting property with a band gap of ∼2.0 eV [10]. The chemical formula for spinel MgFe$_2$O$_4$ can be written as (Mg$_{1-x}$Fe$_x$)A (Mg$_x$Fe$_{2-x}$)B, where, A and B represent the tetrahedral and octahedral vacant sites, respectively, and 'x' is the inversion parameter, which reflects the fraction of iron cations occupying the tetrahedral sites of ferrite structure [11]. Additionally, magnesium ferrite is environmentally friendly, non toxic and cost effective [12]. The electrical and dielectric properties of spinel ferrites can be tuned by varying their structure, surface area, porosity, shape, size, and dimensions through various preparative methods [13,14]. Recently, magnesium ferrite nanoparticles were found to show better properties compared to the bulk. Different synthesis methods, such as hydrothermal, sol-gel, co-precipitation, combustion, etc., have been used to prepare magnesium ferrite nanoparticles in various sizes, shapes and morphologies [7,15–17]. Among them, combustion is found to be simple, cost effective and low temperature synthesis process to obtain good homogeneity of the end product [17]. The key parameter in combustion synthesis is the control of the fuel to oxidant ratio, which favors the constituents to form high degree of pure end product [7,15–17]. Sivakumar et al. prepared MgFe$_2$O$_4$ nanoparticles through the ceramic method followed by high energy ball milling and studied the effect of grain size on electrical and magnetic properties at different frequencies and temperatures

* Corresponding author.
E-mail address: nallanis2011@gmail.com (N. Satyanarayana).

[18]. Doroftei et al. group synthesized Mo and Sn substituted MgFe$_2$O$_4$ nanoparticles through self-combustion method and studied the effect of Mo and Sn substitution on humidity sensitivity of MgFe$_2$O$_4$ nanoparticles [19]. As reported by Santi et al. group, the MgFe$_2$O$_4$ nanofibers prepared by electrospinning method exhibited a magnetic moment of 17.0, 20.7, 25.7 and 31.1 emu/g at 10 KOe, respectively, for the samples obtained at 500, 600, 700 and 800 °C [6]. Ghelev et al. prepared MgFe$_2$O$_4$ particles through auto-combustion method and reported structural and magnetic properties of MgFe$_2$O$_4$ sample [20]. Recent reports revealed that the mesoporous nanocrystalline ferrites exhibited better electrical, dielectric and electrochemical properties [21,22]. To the best of our knowledge, no reports are available on electrical, dielectric and electrochemical properties of the nanocrystalline mesoporous MgFe$_2$O$_4$ particles. Hence, in the present work, nanocrystalline mesoporous MgFe$_2$O$_4$ particles were prepared using urea assisted modified citrate combustion process. All the prepared samples were characterized using XRD, FTIR, Raman spectroscopy, FE-SEM and surface area analyzer, respectively, to confirm the formation of nanocrystalline spinel phase, structure, spherical shape morphology, and specific surface area and porosity. D.C. and A.C. electrical conductivities of the MgFe$_2$O$_4$ sample as function of temperature and frequency were investigated by analyzing the measured impedance data. Further, swagelok-type lithium battery was fabricated using the developed nanocrystalline mesoporous MgFe$_2$O$_4$ particles as anode material and its electrochemical performance was evaluated through cyclic voltammetry and charge-discharge cycles measurements.

2. Experimental

2.1. Synthesis of nanocrystalline mesoporous MgFe$_2$O$_4$ particles

The starting materials, such as ferric nitrate (Fe(NO$_3$)$_3 \cdot$ 9H$_2$O, Qualigence India), magnesium nitrate (Mg(NO$_3$)$_2 \cdot$ 6H$_2$O, Loba Chemical Pvt. Ltd., India), ammonia solution (Fisher Scientific), citric acid (Qualigence, India) and urea (Loba Chemical Pvt. Ltd., India) were purchased and all chemicals were used without further purification for the synthesis of mesoporous MgFe$_2$O$_4$ nanoparticles using urea assisted modified citrate combustion process. Magnesium nitrate and ferric nitrate were used as metal ion sources, citric acid and urea were used as fuel additives. Each chemical was separately dissolved in double deionized water and sonicated for 20 min for homogeneous mixing. The ratio of ferric nitrate and magnesium nitrate was maintained as 2:1. The ratio of metal ion sources, citric acid and urea were maintained at 1:1:0.5. All the metal nitrates and fuel additive solutions were mixed under continuous stirring at 60 °C. Then, 3 ml of ammonia solution was added to the above solution to vary the fuel oxidant ratio, which inturn modify the chemical reaction of the synthesis process. Stirring was continued till the formation of viscous polymeric resin gel and the resin was dried at 150 °C for 12 h to obtain foamy polymeric intermediate sample. Further, based on the thermogravimetric analysis (TG)/differential thermal analysis (DTA) results, polymeric intermediate of MgFe$_2$O$_4$ sample was calcined at 700 °C for 2 h to obtain phase pure mesoporous magnesium ferrite nanoparticles.

2.2. Measurements

Thermogravimetric (TG)/differential thermal analysis (DTA) curves of the polymeric intermediate of MgFe$_2$O$_4$ sample were recorded using thermal analyzer instrument (SETARAM TG-DTA/DSC, France), temperature ranging from 26 to 900 °C. Thermal behavior of the polymeric intermediate of MgFe$_2$O$_4$ sample was

obtained from the analysis of the TG/DTA results. Powder X-ray diffraction (XRD) patterns of the MgFe$_2$O$_4$ samples were recorded using PANalytical X'pert PRO MPD X-ray diffractometer with Cu K$_\alpha$ radiation, scanning of 2θ ranges from 10 to 80°. The formation of pure crystalline phase of MgFe$_2$O$_4$ sample was confirmed from the analysis of the XRD pattern. The crystalline size of the MgFe$_2$O$_4$ nanoparticles was calculated using scherrer's formula,

$$D = \frac{0.9\lambda}{\beta\cos\theta} \tag{1}$$

where "λ" is the wavelength of X-ray radiation, "β" is the full width at half maxima (FWHM) and "θ" is the diffracted peak position. Fourier transform infrared spectroscopy (FTIR) spectrum of the MgFe$_2$O$_4$ sample was recorded in the range from 4000 to 400 cm^{-1} with 4 cm^{-1} resolution for 20 scans using 8700 Shimadzu Fourier transform infrared spectrometer. Raman spectrum of the MgFe$_2$O$_4$ sample was recorded at room temperature using Renishaw in Via Raman microscope, equipped with CCD camera and the sample was excited with 10 mW power (514 nm line radiation). The formation of the structural co-ordination of the MgFe$_2$O$_4$ sample was confirmed from the FTIR and Raman spectral results. The size and shape of the prepared MgFe$_2$O$_4$ sample were examined on field-emission scanning electron microscope (FE-SEM, Carl Zeiss, Ultra 55). The specific surface area and porosity of the MgFe$_2$O$_4$ nanoparticles were obtained from the analysis of the recorded N$_2$ adsorption-desorption isotherms at 77 K. In this process, first, sample was degassed at 200 °C for 2 h to remove adsorbed moisture and trapped gases from the sample and recorded N$_2$ adsorption-desorption isotherms at 77 K using Micrometry Gemini VI BET surface area analyzer. The prepared MgFe$_2$O$_4$ sample powder was well grinded and pressed into the form of pellet of 10 mm diameter and 2–3 mm thickness by applying 3–4 tones of hydraulic pressure. To ensure better electrical contact with the electrodes, silver paste was applied on both surfaces of the pellet and platinum wires were used as electrodes. The pellet was kept between the platinum electrodes and measured the impedance data at different temperature starting from RT (Room temperature) to 573 K in steps of 25 K at wide range of frequencies using "NOVOCONTRAL IMPEDANCE ANALYZER". The DC & AC electrical conductivities and dielectric properties of the MgFe$_2$O$_4$ sample were studied by analyzing the measured impedance data at different temperatures using "*winfit*" software. The DC conductivity of the prepared MgFe$_2$O$_4$ sample was calculated using the following formula.

$$\sigma = \frac{t}{(R*A)} Scm^{-1} \tag{2}$$

where "t" is the thickness of the pellet, "R" is the bulk resistance of the sample and "A" is the area of the pellet. The temperature dependent conductivity of the prepared MgFe$_2$O$_4$ sample is fitted to the following Arrhenius equation.

$$\sigma(T) = \frac{\sigma_0}{T}\exp\left(\frac{-Ea}{KT}\right) \tag{3}$$

where σ_0 is the pre-exponential factor, "K" is the Boltzmann constant, "T" is the temperature in kelvin and "E$_a$" is the activation energy of the sample. The dielectric constant (ε'), dielectric loss tangent (tan δ) and AC conductivity ($\sigma_{a.c.}$) of the sample were evaluated using the measured impedance data and dimensions of the sample pellet.

$$\varepsilon = \frac{Cd}{A\varepsilon_0} \tag{4}$$

where ε is the dielectric constant of the material, ε_0 is the dielectric constant of the free space, "C" is the capacitance of the

sample, d is the thickness of the sample pellet, and "A" is the area of the sample pellet. ε' and ε'' are the real and imaginary parts of the dielectric constant (ε). The dielectric constant (ε'), dielectric loss (ε'') and dielectric loss tangent (tan δ) of the sample can be expressed by the following equations.

$$\varepsilon' = \frac{t}{wRA}\left[\frac{Z''}{Z'^2 + Z''^2}\right] \qquad (5)$$

$$\varepsilon'' = \frac{t}{wRA}\left[\frac{Z'}{Z'^2 + Z''^2}\right] \qquad (6)$$

$$\tan\delta = \frac{\varepsilon''}{\varepsilon'} \qquad (7)$$

where, ε' is the dielectric constant and ε'' is the dielectric loss. A.C conductivity ($\sigma_{a.c.}$) of the sample was calculated by following relation,

$$\sigma_{a.c.} = \omega\varepsilon'\varepsilon'' \tan\delta \qquad (8)$$

where 'ω' is the angular frequency.

2.3. Electrochemical measurements

For electrochemical studies, composite anode was prepared by mixing 70% of active material ($MgFe_2O_4$ powder), 20% of carbon block and 10% of alginate binder in N-methyl 2 pyrrolidinone solvent. The composite $MgFe_2O_4$ slurry was uniformly coated on a copper foil of thickness 12 μm using doctor blade and dried in a hot air oven at 120 °C for 12 h. The dried copper foil was cut (10 mm diameter) and pressed under 1 tone pressure for 30 s using hydraulic press. The 12 mm diameter size of metallic lithium foil was cut and used as counter electrode material. Then, 1 mol of $LiPF_6$ dissolved in a 1:1 volume ratio of ethylene carbonate & dimethyl carbonate (EC:DMC 1:1 V/V) solution was used as an electrolyte. Celgard-2400 (poly propylene) film was used as a separator (14 mm diameter). Swagelok cell type lithium ion battery was fabricated using the above mentioned electrodes, electrolyte and separator materials in an argon filled glove box. The cyclic voltammetry (CV) curves of the cell were recorded in the potential range 0.0–3 V, at a scan rate of 0.1 mV S^{-1}, on Bio-Logic instrument. The charge/discharge measurements of the fabricated swagelok cell type lithium battery were made at a current density of 300 mA/g, on BITRODE (U.S.A) battery cycle tester (BCT).

3. Results and discussion

3.1. TG/DTA

Fig. 1 shows the TG/DTA curves of the polymeric intermediate of $MgFe_2O_4$ sample prepared using the urea assisted modified citrate combustion process. From Fig. 1, in the TGA curve, 12% weight loss is observed between 26 °C and 110 °C, which may be due to the evaporation of adsorbed moisture and the corresponding endothermic peak is observed in the DTA curve. High percentage, upto 41% of weight loss is observed in the temperature range 180–220 °C and the corresponding exothermic peak is observed in the DTA curve. This may be due to the simultaneous combustion reaction as well as evaporation of organic residues and ammonium nitrate. As observed from TGA curve, 7% weight loss is observed between 215 °C and 398 °C, which may be due to the decomposition of nitrates from different metal ion sources and the corresponding two broad exothermic peaks are also observed in the
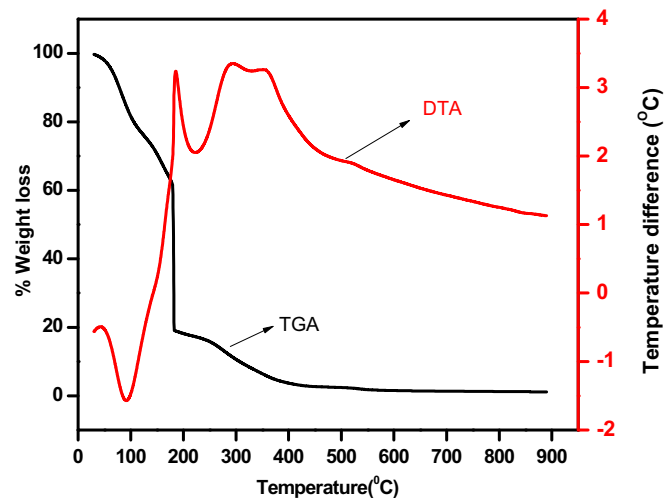

Fig. 1. TG/DTA curves of polymeric intermediate of $MgFe_2O_4$ sample.

DTA curve [23]. Above 550 °C, TGA curve shows no more weight loss and remains 2.52% of weight, which may be due to the formation of the $MgFe_2O_4$ sample and it is further confirms from the XRD results.

3.2. XRD

Fig. 2 shows the XRD pattern of $MgFe_2O_4$ sample obtained at 700 °C along with the JCPDS data. From Fig. 2, the observed diffraction peaks at 2θ of ~18.33, 30.34, 35.6, 37.36, 43.28, 53.68, 57.24, 62.87, 71.08, 74.21 and 78.97 are compared with the standard JCPDS (01-073-2410) data file of $MgFe_2O_4$ and indexed to (111), (220), (311), (222), (400), (422), (440), (511), (620), (533) and (444) respectively. Hence the observed indexed XRD peaks confirm the formation of pure crystalline cubic spinel phase of the magnesium ferrite sample [24]. The crystallite size of the $MgFe_2O_4$ sample is calculated using XRD data and the Scherrer's formula and it is found to be 29.98 nm. Hence, XRD results confirmed the formation of pure nanocrystalline cubic spinel phase of the magnesium ferrite sample.

3.3. FTIR

FTIR spectrum of nanocrystalline mesoporous $MgFe_2O_4$ sample obtained at 700 °C is shown in Fig. 3. From Fig. 3, the observed broad IR band at 3444 cm^{-1} is attributed to the stretching
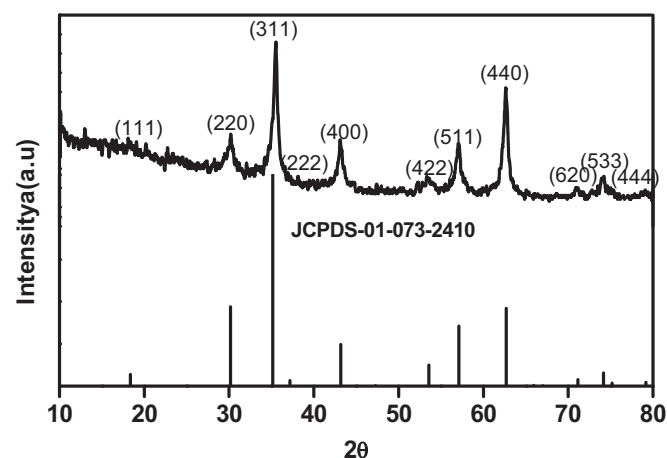

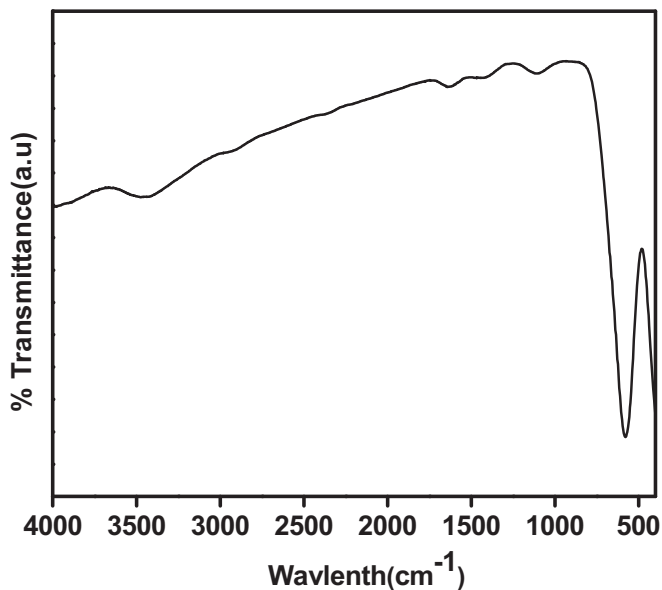**Fig. 2.** XRD pattern of $MgFe_2O_4$ sample obtained at 700 °C.

Fig. 3. FTIR spectrum of MgFe$_2$O$_4$sample obtained at 700 °C.

vibration of structural OH groups and the IR band observed at 1630 cm^{-1} is attributed to the bending vibration of structural OH groups. The IR peaks observed at $\sim$574 cm^{-1} and $\sim$409 cm^{-1} correspond to the stretching vibrations of oxygen atoms and iron cations at tetrahedral and octahedral sites, respectively. Hence, the FTIR results confirmed the formation of MgFe$_2$O$_4$ structure [25].

3.4. Raman spectroscopy

Fig. 4 shows the Raman spectrum of magnesium ferrite sample obtained at 700 °C. The observed Raman spectrum was deconvoluted using the "fit yk" software and obtained clear Raman bands. From Fig. 4, the deconvoluted Raman spectrum of MgFe$_2$O$_4$ sample exhibited bands at 216 cm^{-1}, 329 cm^{-1}, 386 cm^{-1}, 476 cm^{-1}, 644 cm^{-1} and 705 cm^{-1}. The observed Raman bands are assigned based on the structure of the magnesium ferrite. According to the White and De Angelis, spinel ferrites exhibit five – active Raman modes, such as one A$_{1g}$, one Eg and three T$_{2g}$ modes [26]. From Fig. 4, the observed Raman bands at 216 cm^{-1}, 386 cm^{-1} and 476 cm^{-1} are attributed to three T$_{2g}$ modes. Raman peaks observed at 329 cm^{-1} and 705 cm^{-1} are assigned to E$_g$ and A$_g$
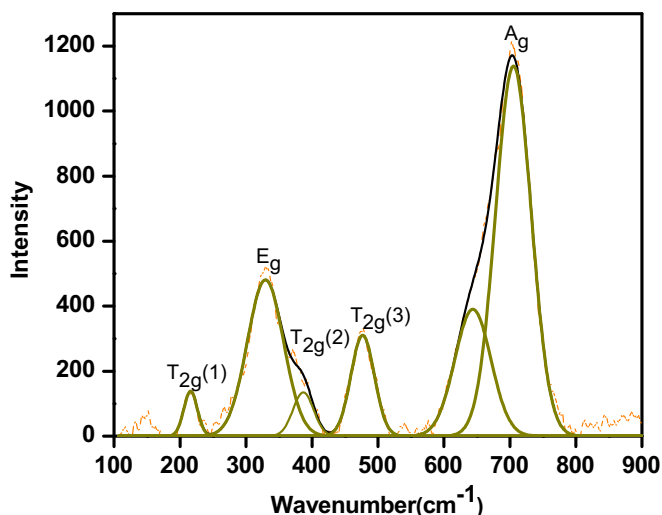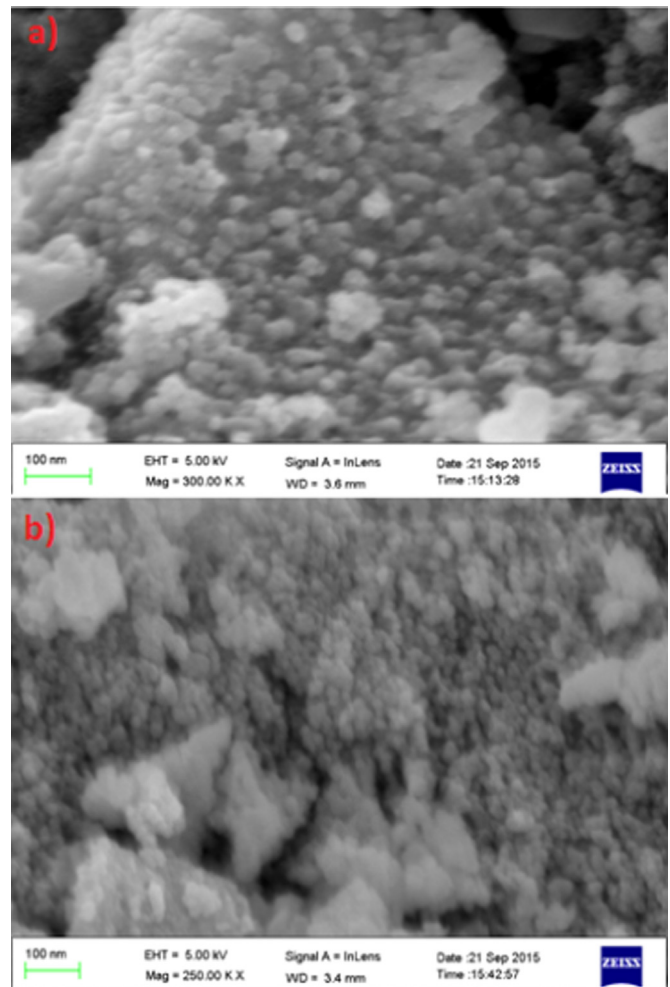

Fig. 5. SEM micrographs of nanocrystalline MgFe$_2$O$_4$ sample.

modes, respectively. The additional Raman band observed at 644 cm^{-1} corresponds to the order – disorder effects of two metal ions over octahedral and tetrahedral sites in magnesium ferrite [27]. Hence, Raman results confirmed the formation of spinel structured magnesium ferrite.

3.5. FE-SEM

Fig. 5 shows the FE-SEM micrographs of MgFe$_2$O$_4$ sample at different magnifications. From Fig. 5, the FE-SEM images show the formation of agglomerated spherical particles and the average particle size is found to be less than $\sim$40 nm. Hence, FE-SEM results confirmed that the prepared MgFe$_2$O$_4$ particles using the urea assisted modified citrate combustion process are spherical in shape with an average particle size less than $\sim$40 nm.

3.6. BET surface area analysis

Fig. 6 shows the N$_2$ adsorption-desorption isotherm curves measured at 77 K for MgFe$_2$O$_4$ powder sample. From Fig. 6, the observed isotherm curves are compared with IUPAC standard curves and confirmed that the prepared MgFe$_2$O$_4$ sample exhibits IVth type isotherm with H$_4$ hysteresis loop, which confirms the formation of mesoporous structured MgFe$_2$O$_4$ sample, prepared using the urea assisted modified citrate combustion process [27]. The observed mesoporous structure of the magnesium ferrite sample may be due to the decomposition of ammonium nitrate and organic residues during the calcination process. The specific
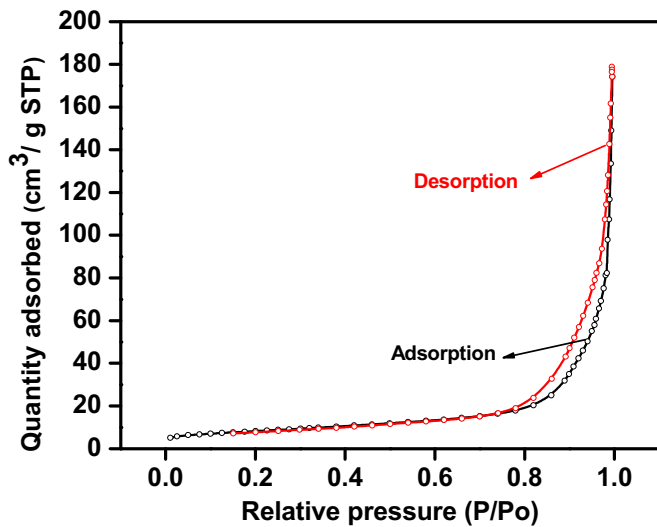

Fig. 4. Raman spectrum of MgFe$_2$O$_4$ sample obtained at 700 °C.

Fig. 6. Nitrogen adsorption-desorption curves of MgFe$_2$O$_4$ sample obtained at 77 K.

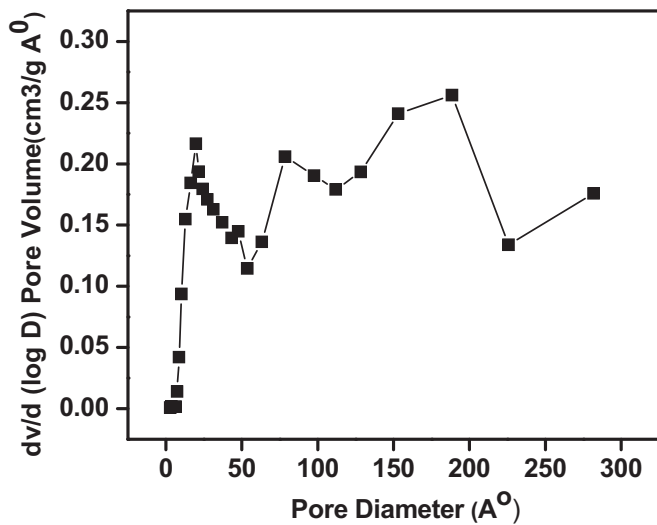**Fig. 7.** Pore size distribution of MgFe$_2$O$_4$ sample obtained at 700 °C.

surface area of magnesium ferrite samples was evaluated using the nitrogen physisorption data and Brunauer-Emmett-Teller (BET) method. Also, the pore size of the magnesium ferrite sample was

evaluated using the nitrogen physisorption data and Barrett-Joyner-Halenda (BJH) desorption method [28]. Specific surface area, pore size and pore volume of the magnesium ferrite sample were respectively, found to be 29.4038 m^2/g, 35.5330 nm and 0.269358 cm^3/g. Fig. 7 shows the pore size distribution of the magnesium ferrite sample. The XRD, Raman, SEM and BET surface area results confirmed the formation of nanocrystalline spinel structured mesoporous magnesium ferrite (MgFe$_2$O$_4$), synthesized using the urea assisted modified citrate combustion process.

3.7. Impedance and conductivity

Fig. 8 (a and b) show the impedance (real Z′ vs. imaginary Z″) plots obtained from RT to 573 K of the nanocrystalline spinel structured mesoporous MgFe$_2$O$_4$ sample. The inset Fig. 8(a) shows the expanded impedance (real Z′ vs. imaginary Z″) plot, deconoluted with grain interior and grain boundary resistance obtained at RT. From Fig. 8, different shapes of points are the measured impedance data and the continuous lines are fitted impedance data of mesoporous MgFe$_2$O$_4$ sample. Also, each impedance plot exhibits two semicircles of arcs at all measured temperatures (shown in inset of Fig. 8(a) for RT). The observed first semicircle of the arc at high frequency side is attributed to the grain interior property of the sample and the second semicircle of the arc at low frequency side is attributed to the grain boundary property of the sample. The measured impedance data was fitted and analyzed using "win fit" software. The grain interior (bulk) resistance, grain boundary resistance and their electrical behavior in terms of an equivalent circuit were evaluated by analyzing the measured impedance data using "winfit" software. The high frequency semicircle of the arc arises due to the parallel combination of bulk resistance (R$_b$) and bulk capacitance (C$_b$) of the MgFe$_2$O$_4$ sample. The low frequency semicircle of the arc arises due to the parallel combination of grain boundary resistance (R$_{gb}$) and grain boundary capacitance (C$_{gb}$) of the MgFe$_2$O$_4$ sample. The total conductivity of the MgFe$_2$O$_4$ sample was calculated using the pellet dimension, resistance value and the conductivity Eq. (2). Fig. 9 shows the temperature dependence of the conductivity (log σT vs. 1000/T) of MgFe$_2$O$_4$ sample and it was fitted to Arrhenius Eq. (3). From Fig. 9, the conductivity decreases with temperature up to 373 K, labeled as region 1 and starts increases linearly with temperature up to 573 K, labeled as region 2. The decreased conductivity with temperature in the region 1 may due to the removal of the absorbed moisture of the sample, which is confirmed from the IR and TG-DTA results. Hence, the observed higher conductivity (1.325 × 10^{-7} S cm^{-1}) at RT is may be due to the protons from the absorbed moisture and
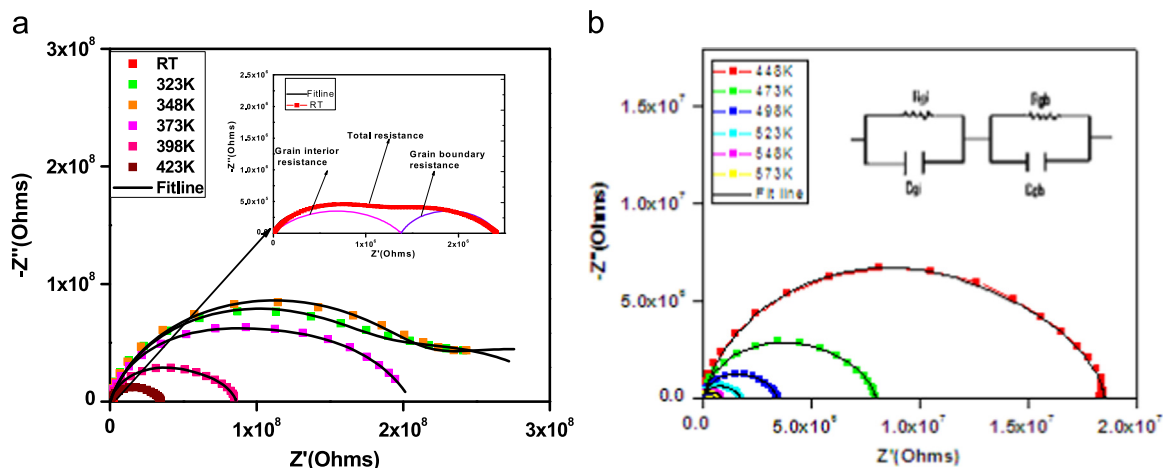

Fig. 8. (a) Impedance spectra obtained at different temperatures (RT – 423 K) of MgFe$_2$O$_4$ sample: inset shows the grain interior, grain boundary and total resistance of MgFe$_2$O$_4$ sample obtained at RT. (b) Impedance spectra obtained at different temperatures (448–573 K) of MgFe$_2$O$_4$ sample.
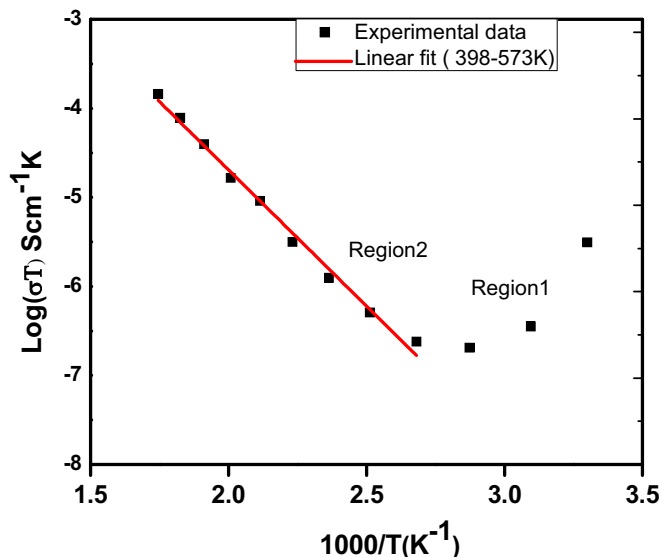
Fig. 9. Log (σT) verses 1000/T (K^{-1}) plot of nanocrystalline mesoporous MgFe$_2$O$_4$ sample.

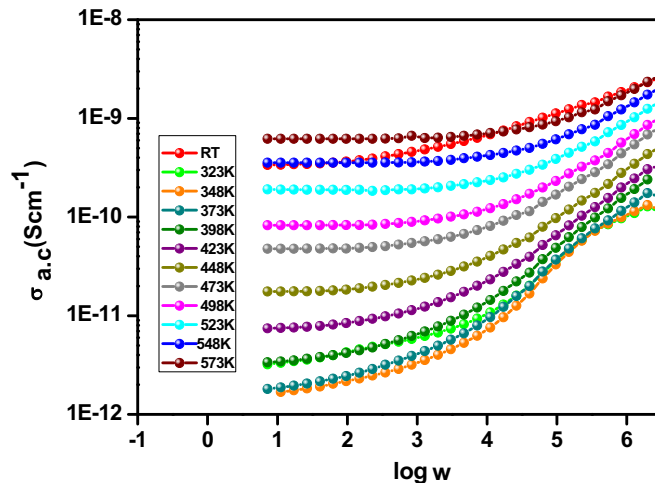**Fig. 10.** a.c. conductivity versus log ω plots obtained at different temperature (RT to 573K) of nanocrystalline mesoporous MgFe$_2$O$_4$ sample.

electrons from the MgFe$_2$O$_4$ sample. The linear increase of conductivity with temperature in the region-2 is may be due to the thermal activation of hopping of electrons between Fe^{+3} and Fe^{+2} ions in the octahedral sites (B sites) of spinel MgFe$_2$O$_4$ structure. The Activation energy (E$_a$) required for the migration of the carriers was evaluated from the slope of the log (σT) vs. 1000/T plot of the MgFe$_2$O$_4$ sample and it is found to be 0.607 eV. The evaluated grain interior, grain boundary and the total electrical conductivities of MgFe$_2$O$_4$ sample are given in Table 1.

3.8. A.C. conductivity

Fig. 10 shows the log (σ$_{ac}$) vs. log (ω) plots of the MgFe$_2$O$_4$ sample obtained at different temperatures (RT to 573 K, in steps of 25 K). From Fig. 10, the log (σ$_{ac}$) vs. log (ω) plots showed two different regions of conductivity, low frequency plateau region and high frequency dispersion region. Also, an extrapolation of low frequency plateau region towards the Y-axis gives the dc conductivity (σ$_{dc}$) of the sample, which is equal to the total or bulk conductivity evaluated from the analysis of the measured impedance data. From Fig. 10, the frequency at which the conductivity changes from low frequency plateau region to high frequency dispersion region is called hopping frequency (ω$_p$). The conductivity mechanism in ferrites is due to the hopping of electrons between Fe^{+3} and Fe^{+2} ions in the octahedral sites (B sites) of spinel ferrite structure. An increase in frequency of the applied

field increases the hopping frequency of electrons, which may increase the mobility of charge carriers. Hence, an observed increase in conductivity with frequency may be due to the enhancement of mobility of the charge carries in the ferrite structure [29–31].

3.9. Dielectric properties

Fig. 11 shows the variation of dielectric constant (ε′) as function of frequency for MgFe$_2$O$_4$ sample, at different temperatures ranging from RT to 573 K. From Fig. 11, it is observed that the dielectric constant increases with decrease of frequency. As the frequency decreases, the charges file up at electrode-electrolyte interface, causing the increase in dielectric constant and hence, it is called interfacial polarization effect. The dielectric constant decreases with increase of frequency, which may be due to the fast hopping of electrons between Fe^{+2}↔Fe^{+3} ions [32,33]. Fig. 12 shows the variation of dielectric loss tangent (tan δ) as function of frequency at different temperatures, ranging from RT to 573 K. From Fig. 12, it is observed that the loss tangent (tan δ) is found to be very high at low frequencies and it decreases with frequency, which may be due to the change of polarity of the charge carriers with the external field beyond certain frequency [34,35].

3.10. Electrochemical performance

3.10.1. Cyclic voltammetry (CV)
Cyclic voltammetry (CV) curves of the developed nanocrystalline mesoporous MgFe$_2$O$_4$ sample for the 1st, 2nd, 3rd and 4th

Table1
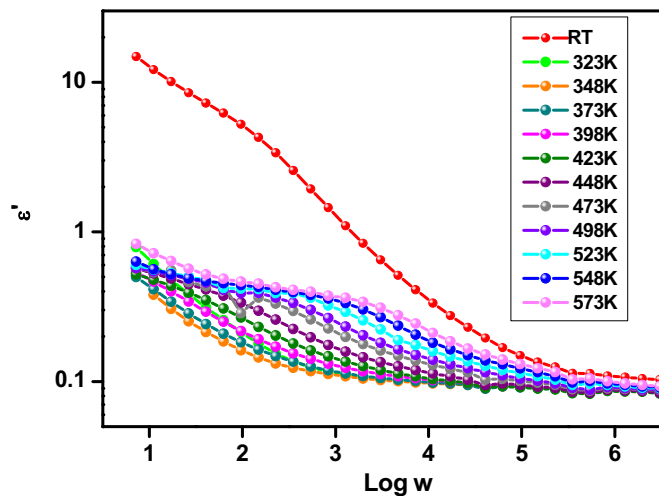Temperature, grain interior conductivity, grain boundary conductivity and total conductivity of MgFe$_2$O$_4$ sample.

S.No.	Temperature (K)	Grain interior conductivity (S cm^{-1})	Grain boundary conductivity (S cm^{-1})	Total conductivity (S cm^{-1})
1	RT	2.33×10^{-7}	3.093×10^{-7}	1.328×10^{-7}
2	323	1.847×10^{-9}	2.382×10^{-9}	1.041×10^{-9}
3	348	1.076×10^{-9}	1.31×10^{-9}	5.9×10^{-10}
4	373	1.214×10^{-9}	1.357×10^{-9}	6.407×10^{-10}
5	398	2.512×10^{-9}	2.635×10^{-9}	1.287×10^{-9}
6	423	6.62×10^{-8}	5.333×10^{-8}	2.954×10^{-9}
7	448	2.629×10^{-8}	9.668×10^{-8}	7.069×10^{-9}
8	473	2.362×10^{-8}	1.056×10^{-7}	1.931×10^{-8}
9	498	4.146×10^{-8}	1.685×10^{-7}	3.327×10^{-8}
10	523	8.65×10^{-8}	6.091×10^{-7}	8.493×10^{-8}
11	548	1.786×10^{-7}	7.109×10^{-7}	1.427×10^{-7}
12	573	4.165×10^{-7}	6.426×10^{-7}	2.53×10^{-7}

Fig. 11. Dielectric permittivity versus log ω plots obtain at different temperature (RT to 573 K) for the nanocrystalline mesoporous MgFe₂O₄ sample.

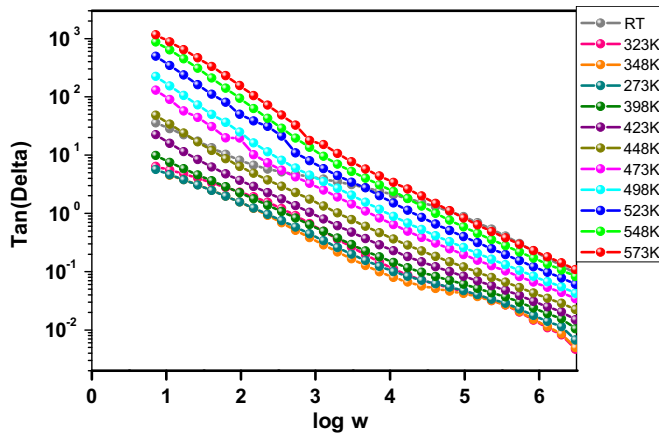**Fig. 12.** Dielectric tangent loss (tan δ) versus log ω plots obtained at different temperature (RT to 573 K) for the nanocrystalline mesoporous MgFe₂O₄ sample.

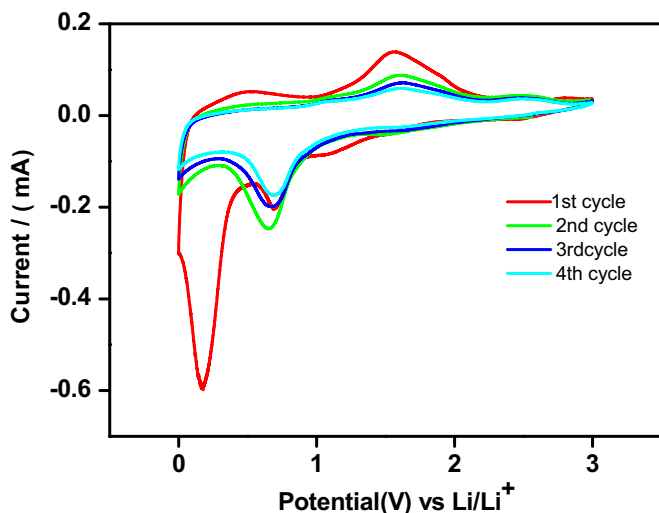**Fig. 13.** Cyclic voltammogram of current versus potential curves for the 1st, 2nd, 3rd and 4th cycles at scan rate of 0.01 mV of lithium battery made up of nanocrystalline mesoporous MgFe₂O₄ sample.

cycles, at a scan rate of 0.1 mV s^{-1}, are shown in Fig. 13. From Fig. 13, for the first cycle, two cathodic peaks are observed; one at 0.18 V and other at 0.69 V. In the subsequent 2nd, 3rd and 4th

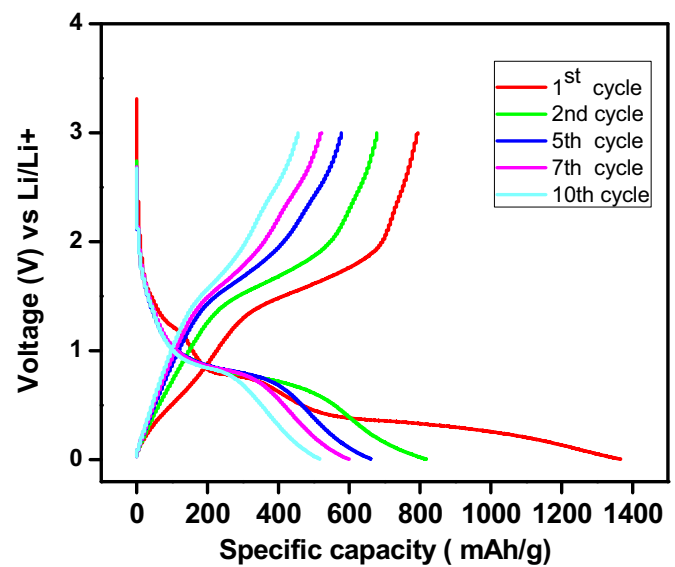**Fig. 14.** Charge/Discharge plots obtained for the 1st, 2nd, 5th, 7th and 10th cycles between the voltage range of 0.005–3 V of lithium battery made up of nanocrystalline mesoporous MgFe₂O₄ sample.

cycles, the first peak observed at 0.18 V was disappeared and the material exhibited only one cathodic peak. The observed first spiky cathodic peak at 0.18 V is attributed to the formation of the solid electrolyte interface (SEI) layer at electrode-electrolyte interface [36]. The observed second cathodic peak at 0.69 V is due to the reduction of Fe^{+3} to Fe^{0} and Mg^{+2} to Mg^{0} of their metallic states. As shown in Fig. 13, mesoporous MgFe₂O₄ sample exhibits one anodic peak at 1.55 V for the 1st cycle, which may be attributed to the oxidation of metals: Fe^{0} to Fe^{+3} and Mg^{0} to Mg^{+2}. The observed decrease in peak intensities and integrated area, from first cycle to subsequent cycles, are attributed to the loss of capacity retention of the material during charge–discharge processes and it is discussed in section 3.10.2 [4,36].

3.10.2. Charge-discharge cycles

Fig. 14 shows the charge-discharge curves of the lithium ion battery fabricated using the newly developed nanocrystalline mesoporous MgFe₂O₄ sample as an anode material, in the voltage range 0.005–3 V, at a current density of 300 mA/g. The first cycle discharge capacity of mesoporous MgFe₂O₄ sample is found to be 1366.6 mAh/g, which is higher than its theoretical capacity (916 mAh/g). The observed high discharge capacity is may be due to the decomposition of organic electrolyte and formation of solid electrolyte interface (SEI) layer at electrode-electrolyte interface for the first cycle [12,36–38]. This is also in accordance with the observed first cathodic peak of CV results shown in Fig. 13. For the subsequent 2nd, 10th and 20th cycles, discharge capacity is respectively found to be 816.6, 516.6 and 411.1 mAh/g. The observed capacity loss for the subsequent cycles may be due to the pulverization and aggregation of MgFe₂O₄ nanoparticles [12]. After 20th cycle, the delivered discharge capacity is about 411.1 mAh/g, which is higher than the theoretical capacity of commercially used graphite (372 mAh/g). Fig. 15 shows the discharge capacity & Coulombic efficiency vs. number of cycles of nanocrystalline mesoporous MgFe₂O₄ material. The coulombic efficiency for the first cycle is 58.1% and the efficiency improved to 92.4% after first cycle. The observed high efficiency is may be due to the mesoporous nature and high surface area of the nanocrystalline MgFe₂O₄ [22]. After 50 cycles, the observed discharge capacity is found to be 316.6 mAh/g, which is better than the early reported values [39]. Hence, newly developed mesoporous MgFe₂O₄ anode material
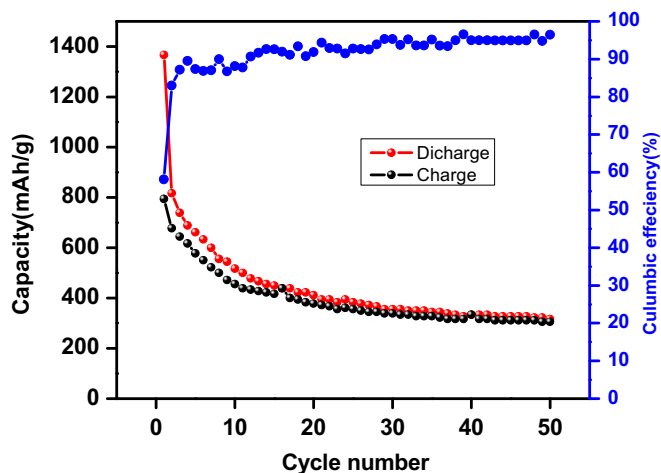
Fig. 15. Discharge capacity & Columbic efficiency verses number of cycles obtained at 300 mA/g of lithium battery made up of nanocrystalline mesoporous $MgFe_2O_4$ sample.

using the urea assisted modified citrate combustion synthesis can be a better anode material for the lithium battery applications.

4. Conclusions

Spinel structured nanocrystalline mesoporous $MgFe_2O_4$ sample was prepared by urea assisted modified citrate combustion process. Thermal behavior of the polymeric intermediate of $MgFe_2O_4$ sample was obtained from the analysis of TG/DTA results. The purity of the phase and structural co-ordination of the $MgFe_2O_4$ sample were respectively confirmed from XRD and FTIR results. Also, the formation of agglomerated spherical particles shape and high surface area of nanocrystalline mesoporous $MgFe_2O_4$ sample were respectively confirmed from SEM and BET surface area results. The observed electrical and dielectric properties of spinel $MgFe_2O_4$ were explained based on the electron hopping mechanism between Fe^{+2} to Fe^{+3} ions in octahedral sites of the spinel magnesium ferrite. The observed electrochemical properties of the fabricated lithium battery indicate that the newly developed mesoporous spinel magnesium ferrite may be a better anode material for lithium battery applications.

References

[1] H.H. Hamdeh, J.C. Ho, S.A. Oliver, R.J. Willey, G. Oliveri, G. Busca, Magnetic properties of partially-inverted zinc ferrite aerogel powders, J. Appl. Phys. 81 (1997) 1851–1857.
[2] E. Finocchio, V. Lorenzelli, M. Trombetta, S.A. Rossini, IR study of alkene allylic activation on magnesium ferrite and alumina catalysts, J. Chem. Soc. Faraday Trans. 92 (1996) 4687–4693.
[3] N.R. Su, P. Lv, M. Li, X. Zhang, M. Li, J. Niu, Fabrication of $MgFe_2O_4$–ZnO heterojunction photocatalysts for application of organic pollutants, Mater. Lett. 122 (2014) 201–204.
[4] Y. Pan, Y. Zhang, X. Wei, C. Yuan, J. Yin, D. Cao, G. Wang, $MgFe_2O_4$ nanoparticles as anode materials for lithium-ion batteries, Electrochim. Acta 109 (2013) 89–94.
[5] Y. Hou, F. Zuo, A. Dagg, P. Feng, A three-dimensional branched cobalt-doped α-Fe_2O_3 Nanorod/$MgFe_2O_4$ heterojunction array as a flexible photoanode for efficient photoelectrochemical water oxidation, Angew. Chem. 125 (2013) 1286–1290.
[6] S. Maensiri, M. Sangmanee, A. Wiengmoon, Magnesium ferrite ($MgFe_2O_4$) nanostructures fabricated by electrospinning, Nanoscale Res. Lett. 4 (2009) 221–228.
[7] C.-P. Liu, M.-W. Li, Z. Cui, J.-R. Huang, Y.-L. Tian, T. Lin, W.-B. Mi, Comparative study of magnesium ferrite nanocrystallites prepared by sol–gel and coprecipitation methods, J. Mater. Sci. 42 (2007) 6133–6138.
[8] S.V. Bangale, D. Patil, S. Bamane, Preparation and electrical properties of nanocrystalline $MgFe_2O_4$ oxide by combustion route, Arch. Appl. Sci. Res. 3 (2011) 1.
[9] V. Khot, A. Salunkhe, N. Thorat, R. Ningthoujam, S. Pawar, Induction heating studies of dextran coated $MgFe_2O_4$ nanoparticles for magnetic hyperthermia, Dalton Trans. 42 (2013) 1249–1258.
[10] H.-C. Wu, O. Mauit, C.Ó. Coileáin, A. Syrlybekov, A. Khalid, A. Mouti, M. Abid, H.-Z. Zhang, M. Abid, I.V. Shvets, Magnetic and transport properties of epitaxial thin film $MgFe_2O_4$ grown on MgO (100) by molecular beam epitaxy, Sci. Rep. 4 (2014).
[11] R. Köferstein, T. Walther, D. Hesse, S.G. Ebbinghaus, Preparation and characterization of nanosized magnesium ferrite powders by a starch-gel process and corresponding ceramics, J. Mater. Sci. 48 (2013) 6509–6518.
[12] S. Permien, S. Indris, M. Scheuermann, U. Schürmann, V. Mereacre, A.K. Powell, L. Kienle, W. Bensch, Is there a universal reaction mechanism of Li insertion into oxidic spinels: a case study using $MgFe_2O_4$, J. Mater. Chem. A 3 (2015) 1549–1561.
[13] C. Kolekar, P. Kamble, S. Kulkarni, A. Vaingankar, Effect of Gd^{3+} substitution on dielectric behaviour of copper–cadmium ferrites, J. Mater. Sci. 30 (1995) 5784–5788.
[14] T. Shinde, A. Gadkari, P. Vasambekar, DC resistivity of Ni–Zn ferrites prepared by oxalate precipitation method, Mater. Chem. Phys. 111 (2008) 87–91.
[15] V. Šepelák, P. Heitjans, K. Becker, Nanoscale spinel ferrites prepared by mechanochemical route: thermal stability and size dependent magnetic properties, J. Therm. Anal. Calorim. 90 (2007) 93–97.
[16] T. Valdés-Solís, P. Tartaj, G. Marbán, A. Fuertes, Facile synthetic route to nanosized ferrites by using mesoporous silica as a hard template, Nanotechnology 18 (2007) 145603.
[17] V. Khot, A. Salunkhe, M. Phadatare, N. Thorat, S. Pawar, Low-temperature synthesis of $Mn_xMg_{1-x}Fe_2O_4$ (x=0–1) nanoparticles: cation distribution, structural and magnetic properties, J. Phys. D: Appl. Phys. 46 (2012) 055303.
[18] N. Sivakumar, A. Narayanasamy, J.-M. Greneche, R. Murugaraj, Y. Lee, Electrical and magnetic behaviour of nanostructured $MgFe_2O_4$ spinel ferrite, J. Alloy. Compd. 504 (2010) 395–402.
[19] C. Doroftei, E. Rezlescu, N. Rezlescu, P. Popa, Microstructure and humidity sensitive properties of $MgFe_2O_4$ ferrite with Sn and Mo substitutions prepared by self-combustion method, J. Optoelectron. Adv. Mater. 8 (2006) 1012.
[20] C. Ghelev, T. Koutzarova, S. Kolev, I. Nedkov, K. Krezhov, D. Kovacheva, B. Blagoev, B. Vertruyen, C. Henrist, R. Cloots, Magnetic properties of nanosized $MgFe_2O_4$ powders prepared by auto-combustion, J Phys.: Conf. Ser. (2012) 012048 (IOP Publishing).
[21] R. Indhrajothi, I. Prakash, M. Venkateswarlu, N. Satyanarayana, Binder effect on the battery performance of mesoporous copper ferrite nanoparticles with grain boundaries as anode materials, RSC Adv. 4 (2014) 44089–44099.
[22] Z. Li, T. Zhao, X. Zhan, D. Gao, Q. Xiao, G. Lei, High capacity three-dimensional ordered macroporous $CoFe_2O_4$ as anode material for lithium ion batteries, Electrochim. Acta 55 (2010) 4594–4598.
[23] R. Indhrajothi, I. Prakash, M. Venkateswarlu, N. Satyanarayana, Lanthanum ion (La^{3+}) substituted $CoFe_2O_4$ anode material for lithium ion battery applications, New J. Chem. 39 (2015) 4601–4610.
[24] W.B. Cross, L. Affleck, M.V. Kuznetsov, I.P. Parkin, Q.A. Pankhurst, Self-propagating high-temperature synthesis of ferrites MFe_2O_4 (M=Mg, Ba, Co, Ni, Cu, Zn); reactions in an external magnetic field, J. Mater. Chem. 9 (1999) 2545–2552.
[25] K. Modi, M. Chhantbar, H. Joshi, Study of elastic behaviour of magnesium ferri aluminates, Ceram. Int. 32 (2006) 111–114.
[26] P. Graves, C. Johnston, J. Campaniello, Raman scattering in spinel structure ferrites, Mater. Res. Bull. 23 (1988) 1651–1660.
[27] Z. Wang, P. Lazor, S. Saxena, H.S.C. O'Neill, High pressure Raman spectroscopy of ferrite $MgFe_2O_4$, Mater. Res. Bull. 37 (2002) 1589–1602.
[28] N. Rezlescu, E. Rezlescu, P. Popa, C. Doroftei, M. Ignat, Comparative study between catalyst properties of simple spinel ferrite powders prepared by self-combustion route, Rom. Rep. Phys. 65 (2013) 1348–1356.
[29] B.N. Rao, O. Padmaraj, D. Narsimulu, M. Venkateswarlu, N. Satyanarayana, AC conductivity and dielectric properties of spinel $LiMn_2O_4$ nanorods, Ceram. Int. 41 (2015) 14070–14077.
[30] E.V. Gopalan, K. Malini, S. Sagar, D.S. Kumar, Y. Yoshida, I. Al-Omari, M. Anantharaman, Mechanism of ac conduction in nanostructured manganese zinc mixed ferrites, J. Phys. D: Appl. Phys. 42 (2009) 165005.
[31] S. Patange, S.E. Shirsath, B. Toksha, S.S. Jadhav, K. Jadhav, Electrical and

magnetic properties of Cr^{3+} substituted nanocrystalline nickel ferrite, J. Appl. Phys. 106 (2009) 023914.

[32] R. Nongjai, S. Khan, K. Asokan, H. Ahmed, I. Khan, Magnetic and electrical properties of In doped cobalt ferrite nanoparticles, J. Appl. Phys. 112 (2012) 084321.

[33] T. Meaz, S. Attia, A.A. El Ata, Effect of tetravalent titanium ions substitution on the dielectric properties of Co–Zn ferrites, J. Magn. Magn. Mater. 257 (2003) 296–305.

[34] R. Devan, B. Chougule, Effect of composition on coupled electric, magnetic, and dielectric properties of two phase particulate magnetoelectric composite, J. Appl. Phys. 101 (2007) 014109.

[35] O. Padmaraj, M. Venkateswarlu, N. Satyanarayana, Structural, electrical and dielectric properties of spinel type $MgAl_2O_4$ nanocrystalline ceramic particles synthesized by the gel-combustion method, Ceram. Int. 41 (2015) 3178–3185.

[36] Y. Xiao, X. Li, J. Zai, K. Wang, Y. Gong, B. Li, Q. Han, X. Qian, $CoFe_2O_4$-graphene nanocomposites synthesized through an ultrasonic method with enhanced performances as anode materials for Li-ion batteries, Nano-Micro Lett. 6 (2014) 307–315.

[37] B.N. Rao, P.R. Kumar, O. Padmaraj, M. Venkateswarlu, N. Satyanarayana, Rapid microwave assisted hydrothermal synthesis of porous α-Fe_2O_3 nanostructures as stable and high capacity negative electrode for lithium and sodium ion batteries, RSC Adv. 5 (2015) 34761–34768.

[38] Y. Yin, N. Huo, W. Liu, Z. Shi, Q. Wang, Y. Ding, J. Zhang, S. Yang, Hollow spheres of $MgFe_2O_4$ as anode material for lithium-ion batteries, Scr. Mater. 110 (2016) 92–95.

[39] A.K. Rai, T.V. Thi, J. Gim, J. Kim, Combustion synthesis of $MgFe_2O_4$/graphene nanocomposite as a high-performance negative electrode for lithium ion batteries, Mater. Charact. 95 (2014) 259–265.